Angewandte Chemie
Eine Zeitschrift der Gesellschaft Deutscher Chemiker

Supporting Information

Superconductivity in an Orbital-Reoriented SnAs Square Lattice: A Case Study of $Li_{0.6}Sn_2As_2$ and NaSnAs

J. Wang, T. Ying, J. Deng, C. Pei, T. Yu, X. Chen, Y. Wan, M. Yang, W. Dai, D. Yang, Y. Li, S. Li, S. Iimura, S. Du, H. Hosono, Y. Qi*, J.-g. Guo**

Contents

1. Experimental Procedures

Stoichiometric Li lump, Sn grain, and As powder were weighted in glove box and loaded into an alumina crucible, sealed into an evacuated quartz tube. The tube was then gradually heated to 925 K with duration of 20 hours. The pre-reacted sample was reground, pelletized and heated to 900 K for another 20 hours to achieve homogeneity. Self-flux technique was used to grown $Li_{0.6}Sn_2As_2$ single crystals. The sealed quartz tube was heated to 1200 K in 20 hours, slowly cooled to 1000 K with a rate of 4 K/h, and naturally cooled down to room temperature. Single crystal with size of 1.5 ×1.5 ×0.1 mm^3 can be obtained. NaSnAs single crystal was synthesized following this procedure.

2. Characterizations

Powder X-ray diffraction (PXRD) data were collected using a PANalytical X'Pert PRO diffractometer (Cu K*α* radiation) with a graphite monochromator in a reflection mode. Rietveld refinements of PXRD pattern were performed using the Fullprof software. The composition of Sn and As was determined by Energy Dispersive Spectroscopy (EDS) and inductively coupled plasma atomic emission spectroscopy (ICP-AES). Electrical resistivity and Hall resistivity were measured through the standard four-wire method in the physical property measurement system (PPMS-9T, Quantum Design). *In-situ* high-pressure electrical transport measurements were carried out using a diamond anvil cell (DAC) with the facet diameter of 300 μm. The cubic boron nitride (cBN) powders were employed as pressure transmitting medium and insulating material. Before and after each run, the pressure was measured using the ruby fluorescence method. *In-situ* high-pressure synchrotron XRD experiments were performed at the 4W2 station of the Beijing Synchrotron Radiation facility (BSRF) with a wavelength of 0.6199 A˚ (20 keV) and the spot size of 35 *μ*m × 12 *μ*m.

3. Theoretical calculations

First-principles calculations were carried out with the density functional theory (DFT) implemented in the Vienna ab initio simulation package (VASP)[1],[2]. The generalized gradient approximation (GGA) in the form of Perdew-Burke-Ernzerhof (PBE)[3] was adopted for the exchange-correlation potentials. We used the projector augmented-wave (PAW)[4] pseudopotentials with a plane wave energy of 800 eV; $2s^2 2p^6 3s^1$, $1s^2 2s^1$, $4d^{10} 5s^2 5p^2$ and $3d^{10} 4s^2 4p^3$ were treated as valence electrons for Na, Li, Sn and As, respectively. A Monkhorst-Pack Brillouin zone sampling[5] grid with a resolution of 0.02 ×2π $Å^{-1}$ was applied. The self-consistent field procedure was considered convergent when the energy difference between two consecutive cycles was lower than 10^{-6} eV. Atomic positions and lattice parameters were fully relaxed till all the forces on the ions were less than 10^{-2} eV/Å. Phonon spectra were calculated on 5×5×1 and 5×5×2 supercells for high pressure phase of $LiSn_2As_2$ and NaSnAs using the finite displacement method implemented in the PHONOPY code[6] to determine the lattice dynamical stability of the structures. The Crystal Orbital Hamilton Population (COHP) analysis was carried out with LOBSTER package[7]. The structural searches and predictions were performed with the particle swarm optimization (PSO) technique implemented in the CALYPSO code.

.

4. Additional experimental and computational data of $Li_{0.6}Sn_2As_2$ and NaSnAs

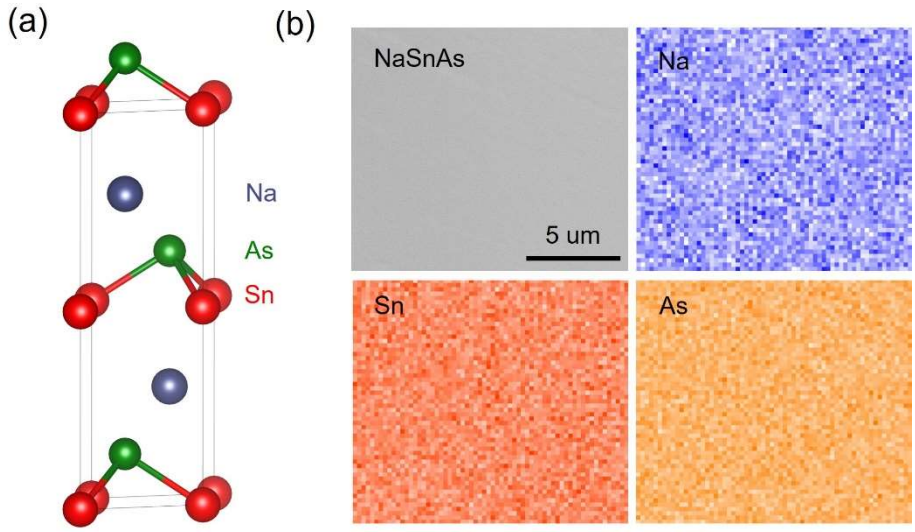

Figure S1 Crystal structure and elemental composition analysis of NaSnAs. (a) Schematic representation of the crystal structure of NaSnAs. (b) SEM image of NaSnAs and elemental mapping of Na, Sn, and As of NaSnAs.

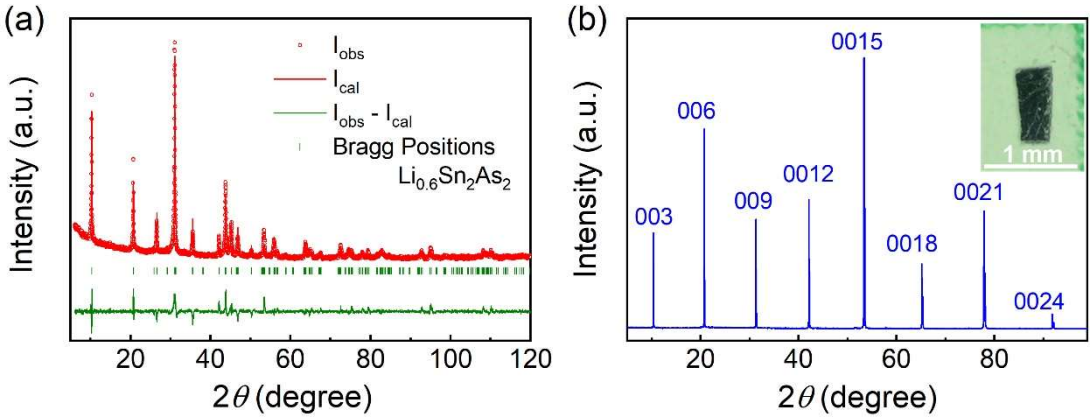

Figure S2 X-ray diffraction results of $Li_{0.6}Sn_2As_2$ powder and single crystal. (a) Rietveld refinements of powder X-ray diffraction (PXRD) pattern of $Li_{0.6}Sn_2As_2$ measured at 300 K. (b) XRD pattern of $Li_{0.6}Sn_2As_2$ single crystal. Inset is the optical image of $Li_{0.6}Sn_2As_2$ single crystal.

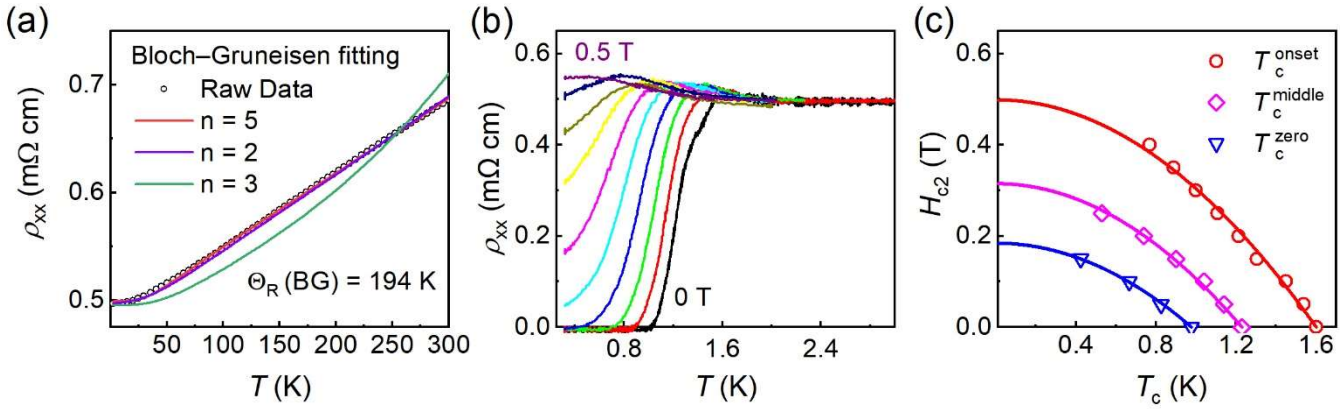

Figure S3 Characterization of electrical transportation of $Li_{0.6}Sn_2As_2$. (a) Resistivity of the $Li_{0.6}Sn_2As_2$ single crystal from 2 to 300 K, the circles represent raw data and the solid lines are Bloch-Gruneisen fitting curve with n=2,3 and 5. (b) Low-temperature resistivity at different magnetic fields parallel to the c axis. (c) The upper critical fields fitted by H_c^{onset},H_c^{middle} and H_c^{zero} with H//c axis.

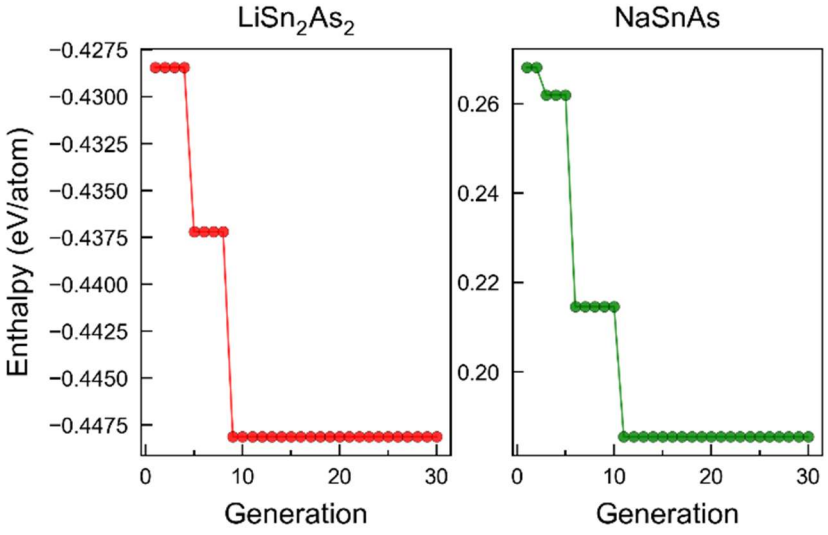

Figure S4 Enthalpy evolution as a function of generation for $LiSn_2As_2$ (left) and NaSnAs (right) at 30 GPa.

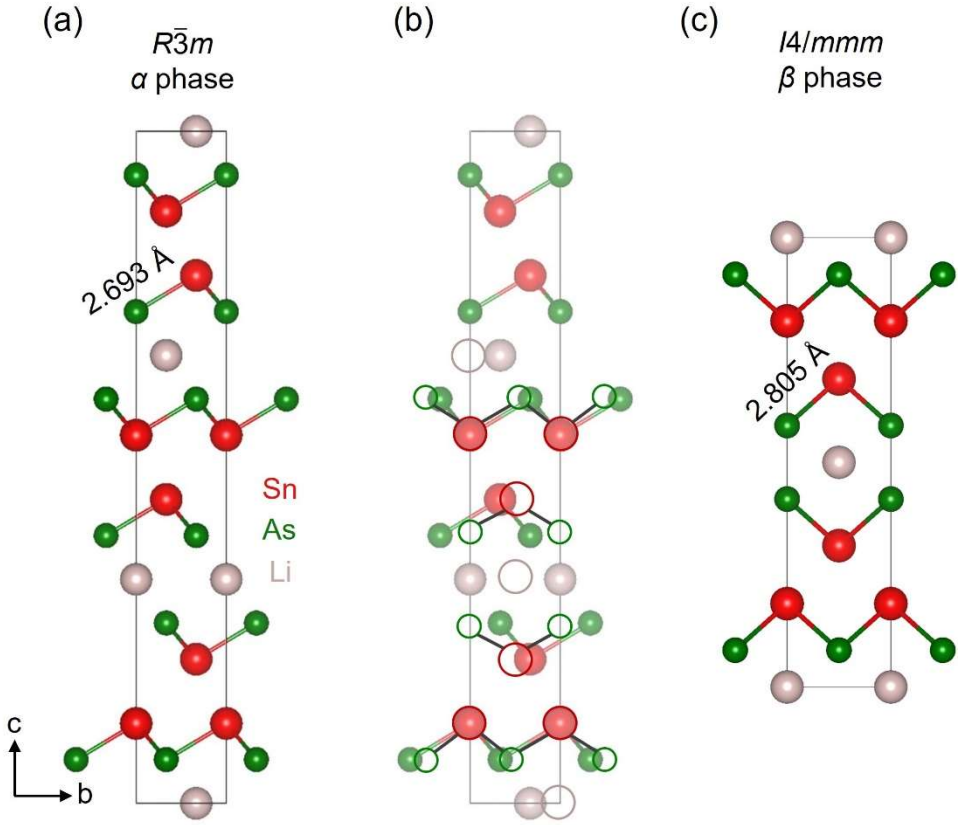

Figure S5 Schematic diagram of the structure evolution of $LiSn_2As_2$. (a) *α* phase ($R\bar{3}m$). (b) Illustration of the structural transformation from *α* phase (solid balls) to *β* phase (open circles). (c) *β* phase (*I*4/*mmm*). Light pink, red, and green balls are Li, Sn, , and As atoms, respectively.

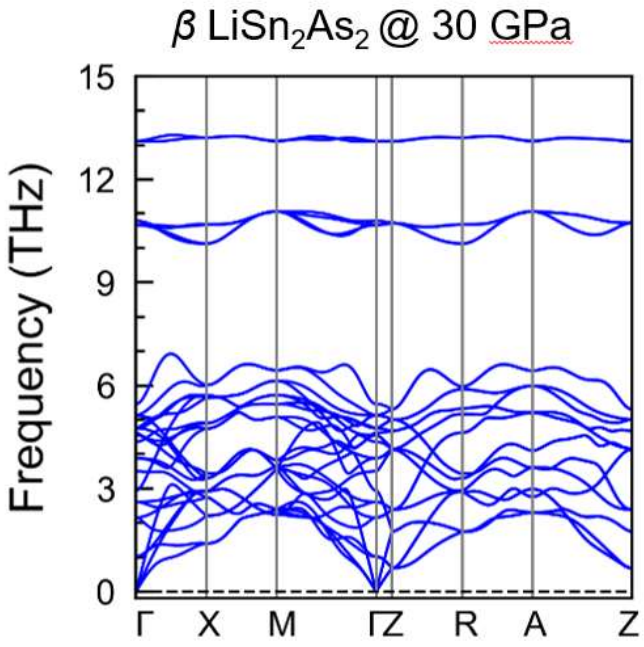

Figure S6 Phonon spectra of β-$LiSn_2As_2$ at 30 GPa.

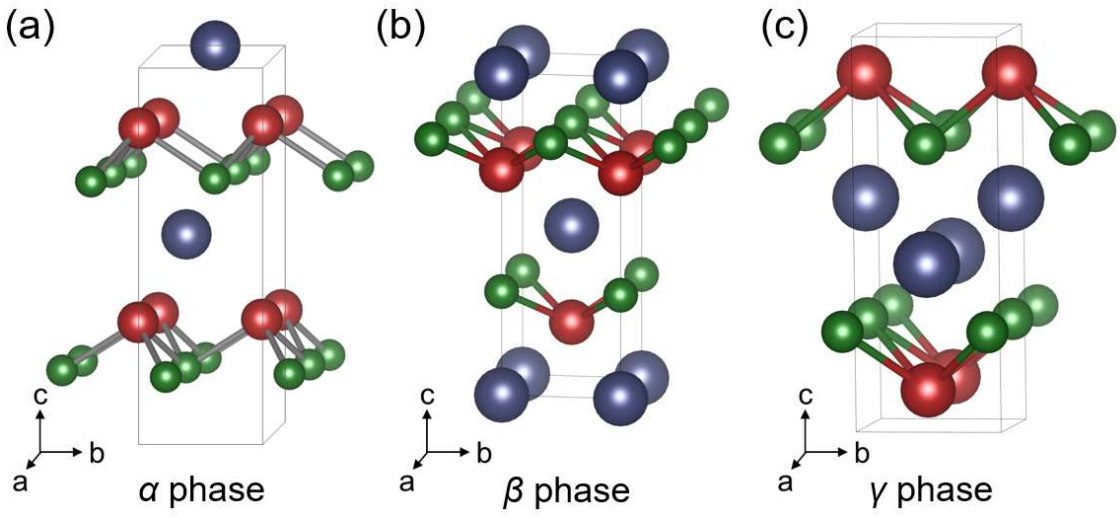

Figure S7 Crystal structures of NaSnAs in different phases. (a) $P6_3mc$ (α phase). (b) $I4/mmm$ (β phase). (c) $P4/mmm$ (γ phase).

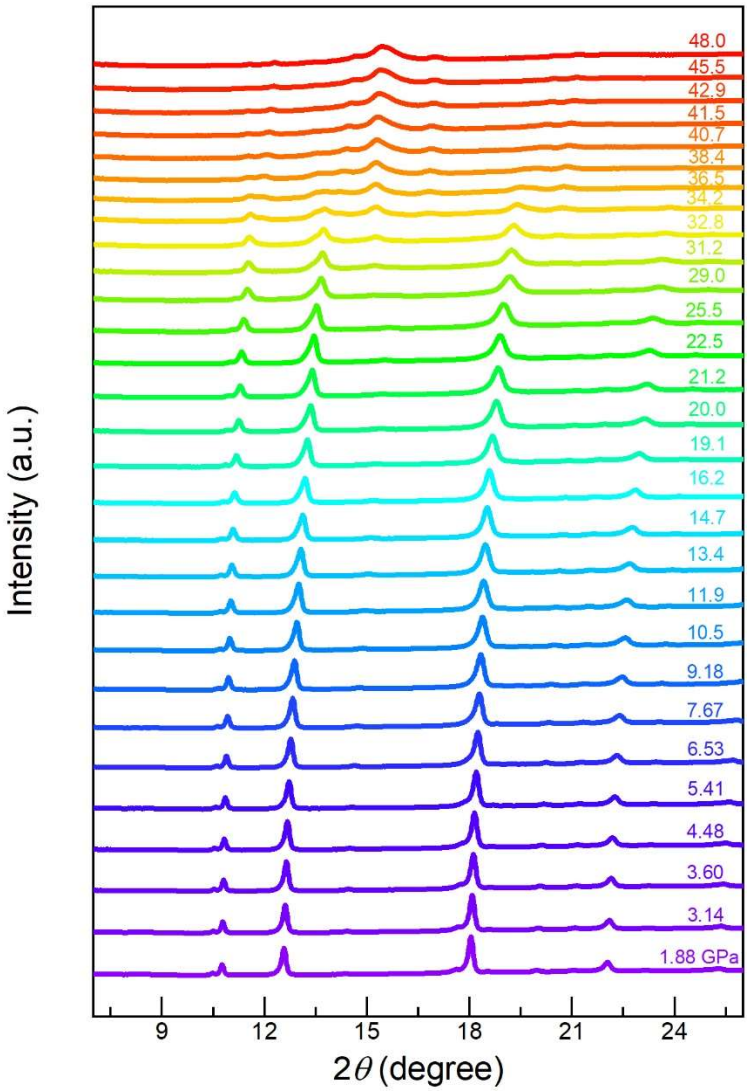

Figure S8 Synchrotron radiation diffraction patterns of $Li_{0.6}Sn_2As_2$ under different pressures.

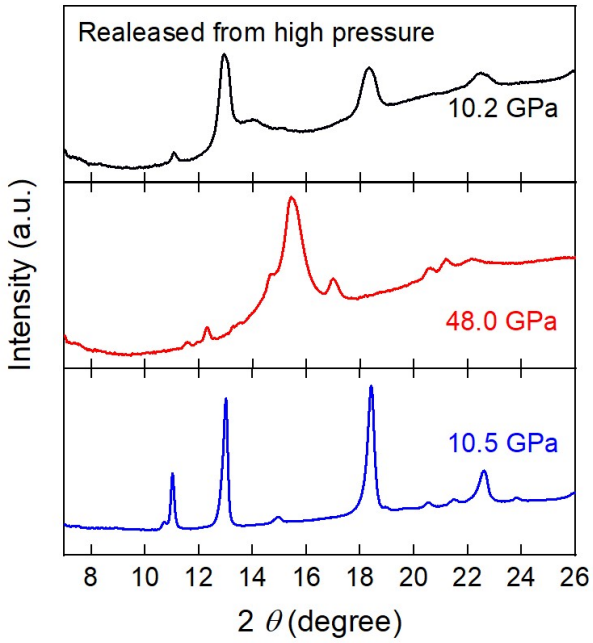

Figure S9 Comparison of synchrotron diffraction patterns of $Li_{0.6}Sn_2As_2$ under different pressures. The blue and red spectra show the diffraction patterns of pressurized process. The black curve shows the diffraction pattern of depressurized $Li_{0.6}Sn_2As_2$ from high pressure.

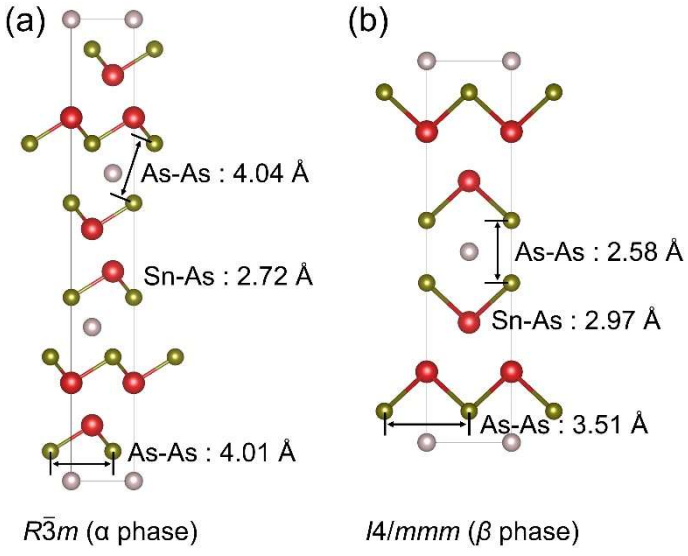

Figure S10 The distances of Sn-As and As-As in (a) $R\bar{3}m$ (α phase) and (b) $I4/mmm$ (β phase) of $LiSn_2As_2$.

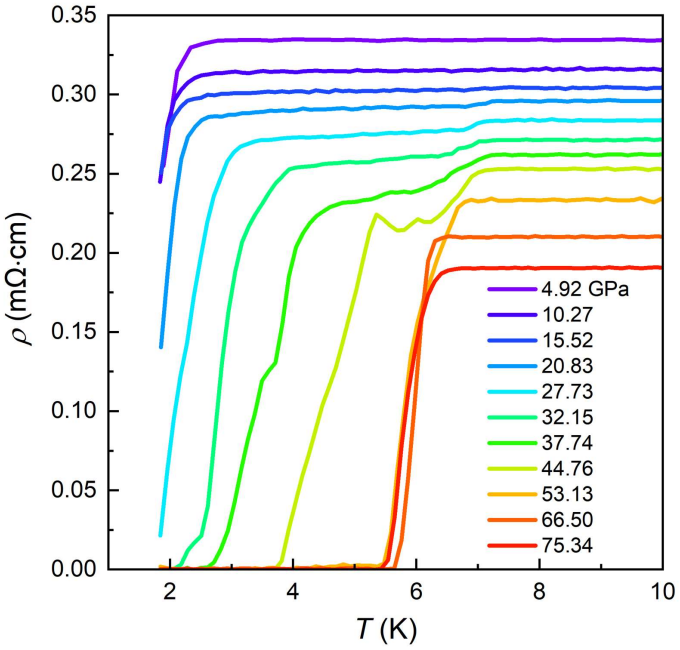

Figure S11 Raw data of pressure-dependent superconductivity in $Li_{0.6}Sn_2As_2$.

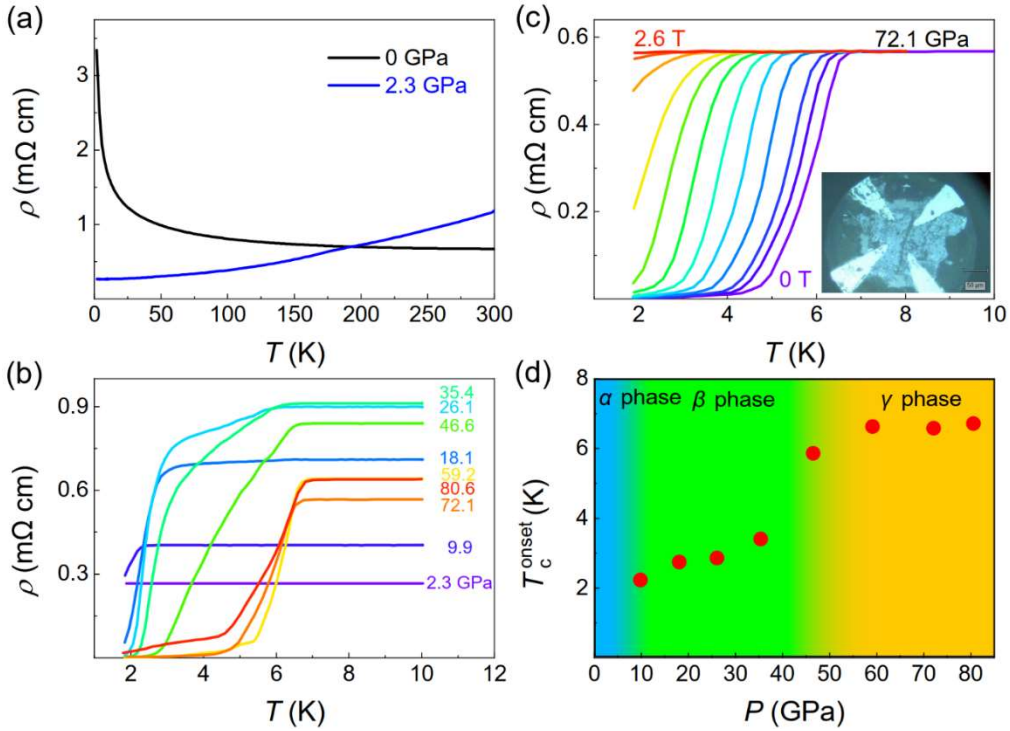

Figure S12 Characterization of electrical transport of NaSnAs under pressure. (a) Temperature dependent resistivity of NaSnAs at ambient pressure (*P* = 0 GPa) and 2.3 Gpa, which shows electrical transport properties of NaSnAs transforming from semiconductor into metal. (b) Pressure-dependent superconductivity of NaSnAs with the applied external pressure. (c) Temperature dependence of the resistivity measured at different magnetic fields under *P* = 72.1 GPa. The inset shows the optical image of NaSnAs sample inside the Diamond Anvil Cell. (d) T_c^{onset} as a function of pressure. *α* phase refers to semiconducting phase, *β* and *γ* phase are two successive superconducting phases.

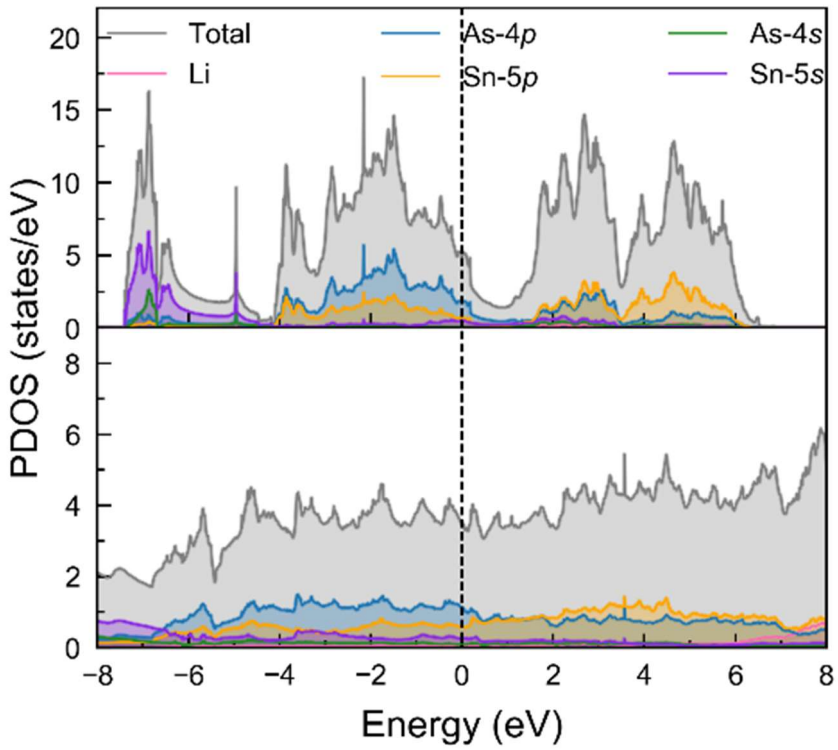

Figure S13 PDOS for $R\bar{3}m$ (α phase) (upper panel) and $I4/mmm$ (β phase) (lower panel) phases of $LiSn_2As_2$.

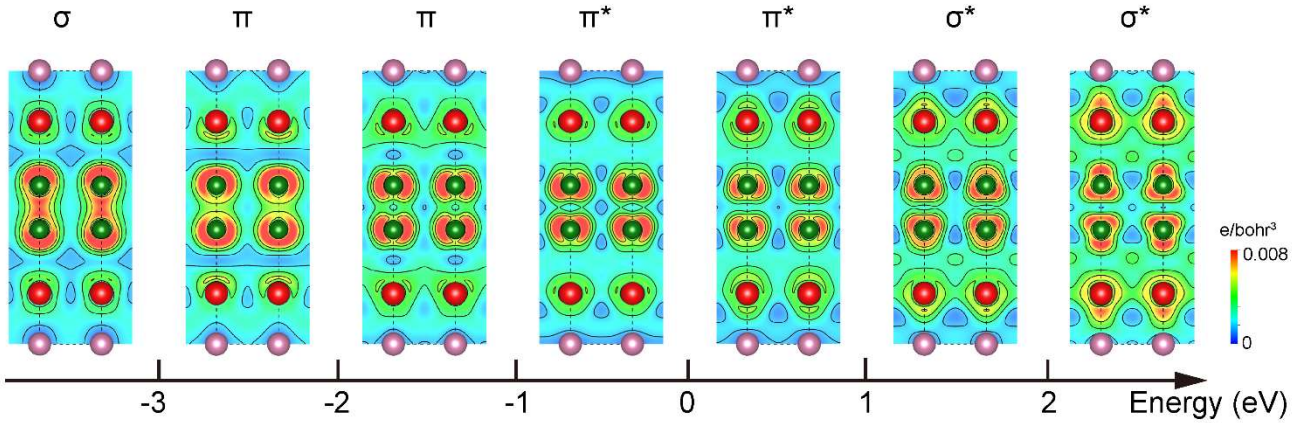

Figure S14 The evolution of electron dispersion with the electron filling from the lowest occupied σ_z bond to the σ_z^* out-of-plane As-As bond of $LiSn_2As_2$.

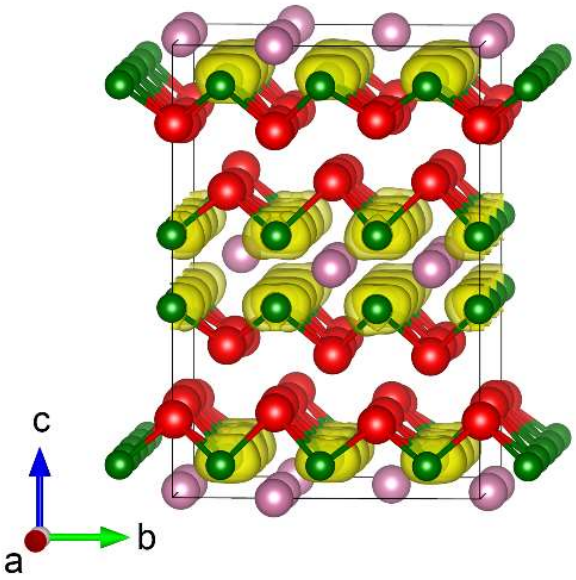

Figure S15 Partial charge density of $Li_{0.6}Sn_2As_2$ at 30 GPa near E_F (|E| < 0.2 eV) with iso-surface value 0.0025 e/Bohr^3.

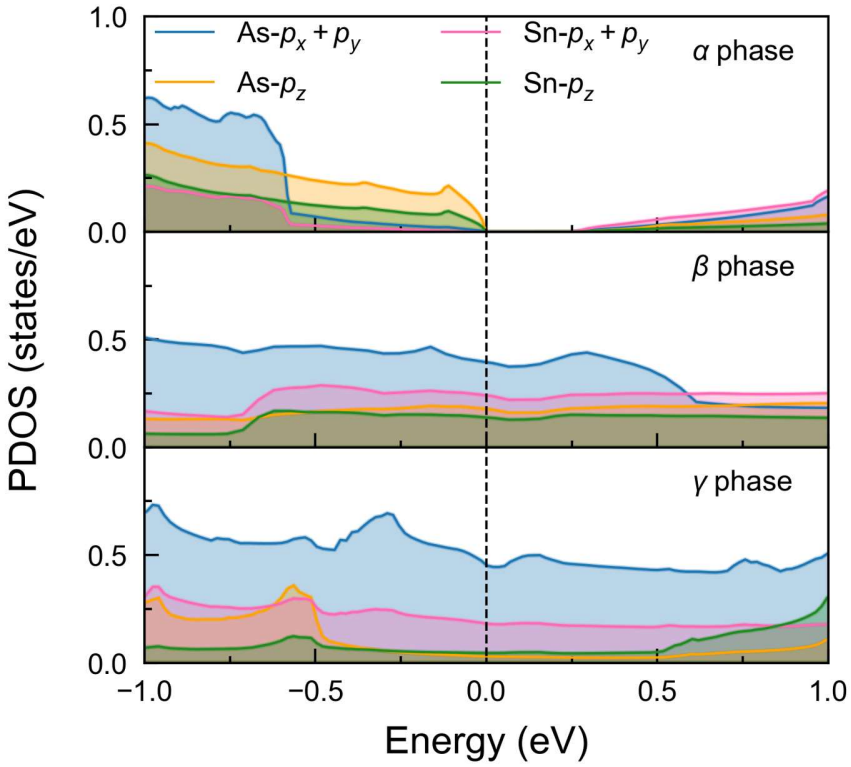

Figure S16 PDOSs of *α*, *β*, and *γ* phase of NaSnAs.

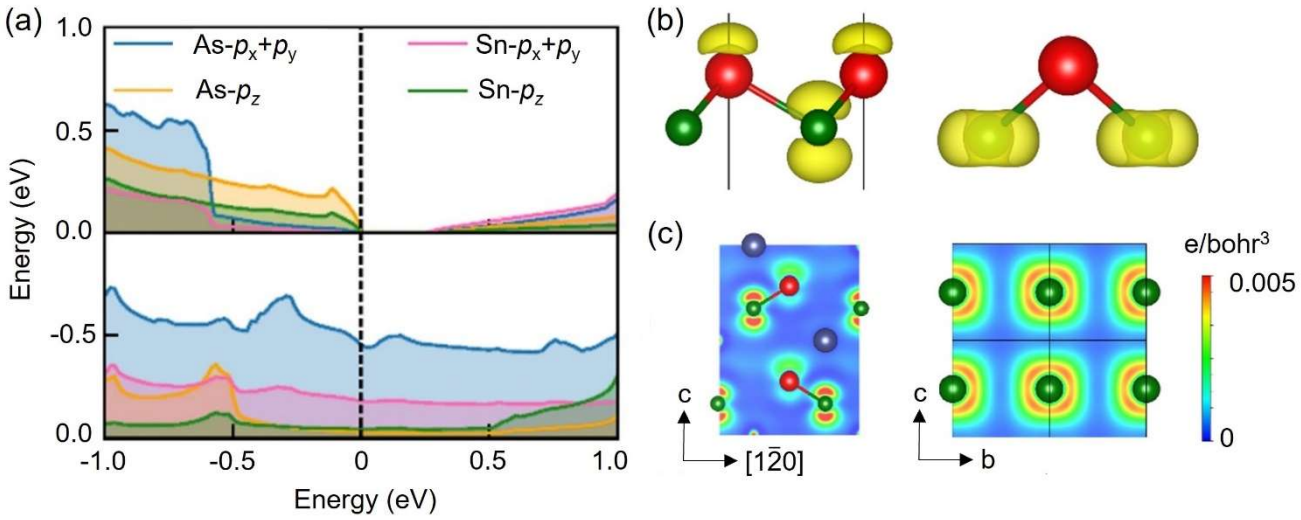

Figure S17 Charge redistribution and orbital reorientation of $SnAs_3$-$SnAs_4$ transformation in NaSnAs. (a) Projected density of states (PDOS) and (b) Partial charge density of *P*6@0 GPa (left panel) and *P*4@30 GPa (right panel) near E_F ($|E| < 0.2$ eV) with iso-surface value of 0.0002 e/Bohr^3 and 0.002 e/Bohr^3, respectively. (c) [1$\bar{2}$0] and [001] slice of the corresponding partial charge density in (b).

5. References

[1]. G. Kresse; J. Furthmuller , Efficiency of ab-initio total energy calculations for metals and semiconductors using a plane-wave basis set. *Comput. Mater. Sci.* **1996,** *6* (1), 15-50.

[2]. G. Kresse; J. Furthmuller, Efficient iterative schemes for ab initio total-energy calculations using a plane-wave basis set. *Phys. Rev. B* **1996,** *54* (16), 11169-11186.

[3]. J. P. Perdew, K. Burke, M. Ernzerhof, Generalized gradient approximation made simple. *Phys. Rev. Lett.* **1996,** *77* (18), 3865-3868.

[4]. G. Kresse, D. Joubert , From ultrasoft pseudopotentials to the projector augmented-wave method. *Phys. Rev. B* **1999,** *59* (3), 1758.

[5]. H. J. Monkhorst; J. D. Pack, Special points for brillouin-zone integrations. *Phys. Rev. B* **1976,** *13* (12), 5188-5192.

[6]. A. Togo; I. Tanaka, First principles phonon calculations in materials science. *Scripta Materialia* **2015,** *108*, 1-5).

[7]. R. Nelson; C. Ertural; J. George, V. L. Deringer; G. Hautier; R. Dronskowski, LOBSTER: Local orbital projections, atomic charges, and chemical-bonding analysis from projector-augmented-wave-based density-functional theory. *Journal of Computational Chemistry* **2020,** *41* (21), 1931-1940.

.